Chemical Engineering Journal 486 (2024) 150031

Contents lists available at ScienceDirect

Chemical Engineering Journal

journal homepage: www.elsevier.com/locate/cej

A continuous flow reactor for tubular gas diffusion electrodes

Nils Weber [a], Max Möntmann [a], Matthias Wessling [a,b], Robert Keller [a,*]

[a] RWTH Aachen University, Aachener Verfahrenstechnik - Chemical Process Engineering, Forckenbeckstr. 51, 52074 Aachen, Germany
[b] DWI - Leibniz Institute for Interactive Materials, Forckenbeckstr. 50, 52074 Aachen, Germany

ARTICLE INFO

Keywords:
CO_2 reduction
Reactor design
Additive manufacturing
Selective laser melting
Hollow fiber electrode
Membrane electrode assembly

ABSTRACT

Tubular gas diffusion electrodes (GDEs) have been mainly characterized in H-cell environments without consideration of changing flow conditions and scale-up possibilities. In this study, a continuous flow reactor for tubular GDEs is presented, which allows for different electrode configurations and manipulation of flow conditions to control mass transfer. 3D printed copper GDEs are employed for CO_2 electroreduction while membrane electrode assemblies (MEAs) from stainless steel electrodes are used on the anode side. We demonstrate the impact of the gas supply in either flow-through or flow-by mode on catalyst performance. Flow-through mode yields a variety of typical products, such as CO, HCOOH, CH_4 and C_2H_4. Flow-by mode results in mainly CH_4, which we link to a higher surface coverage of reaction intermediates with diffusion as the governing transport mechanism in flow-by operation. Additionally, a hybrid porosity GDE is introduced that combines different functional domains in one electrode for improved CO_2 mass transfer. Microcomputed tomography confirms the successful realization of these domains in close proximity to each other. With the presented approach, we aim to highlight the importance of the reaction environment for an effective scale-up of tubular concepts in CO_2 electroreduction and many other electrochemical applications.

1. Introduction

CO_2 electroreduction may contribute to the transformation of the chemical industry towards renewable routes for a variety of different chemicals [1]. Using CO_2 as a feedstock together with renewable electricity, CO_2 electroreduction opens up possibilities for the climate-friendly synthesis of platform chemicals and alternative fuels [2].

Aside from commonly reported planar gas diffusion electrodes (GDEs), tubular GDEs for CO_2 electroreduction emerged in the last years and showed promising results. From the first work by Kas et al. in 2016 [3], numerous groups have been dedicated to the production of tubular GDEs, also referred to as hollow fiber electrodes. Different materials have been investigated and characterized regarding their electrocatalytic performance.

Publications cover electrodes made from copper [4–10], electrodes from copper and tin [11–13] and copper electrodes plated with silver [12], gold or nickel [14]. Apart from that, copper electrodes were prepared with different bronze phases [15] and functionalized with bismuth-based nanosheets [16] or copper nanocubes [17] to tune product selectivity. Further works focused on nickel electrodes treated with zeolite confined bismuth nanoparticles [18] and carbon nanotubes incorporated with either tin [19] or tin oxide nanoparticles [20]. In an alternative approach, nickel electrodes were coupled with CO_2 metabolizing microorganisms for microbial electrosynthesis of acetate and methane (CH_4) [21–23]. Moreover, silver hollow fiber electrodes were presented for the selective production of carbon monoxide (CO) [24–26] and multicarbon products [27] at high current densities.

Just recently, we introduced tubular copper GDEs produced via selective laser melting (SLM) [28]. By engineering the laser hatching strategy, the pore network was manipulated regarding porosity, pore diameter and electrochemically active surface area (ECSA). This in turn allowed for boosting the CO_2 reduction reaction (CO_2RR) while mitigating the competing hydrogen evolution reaction (HER). In another work, we showed how 3D printed porous electrodes can be incorporated into a tubular reactor, thereby improving mass transfer of reactants to the catalyst surface [29].

In spite of numerous publications dealing with tubular GDEs for CO_2-related applications, reports on suitable reactor concepts are rare [12,30,31]. CO_2 electroreduction with tubular GDEs has been almost entirely limited to H-cell environments. For planar plate-and-frame systems, however, electrochemical flow cells are well-established and have been widely used [32–34]. Many studies have demonstrated the impact of the reaction environment and the process conditions on electrocatalytic performance and long-term stable operation [35–38]. For this reason, reactor concepts are necessary to characterize tubular GDEs under changing conditions and different flow regimes. Suitable

* Corresponding author.
E-mail address: robert.keller@avt.rwth-aachen.de (R. Keller).

https://doi.org/10.1016/j.cej.2024.150031
Received 10 November 2023; Received in revised form 23 February 2024; Accepted 26 February 2024
Available online 11 March 2024

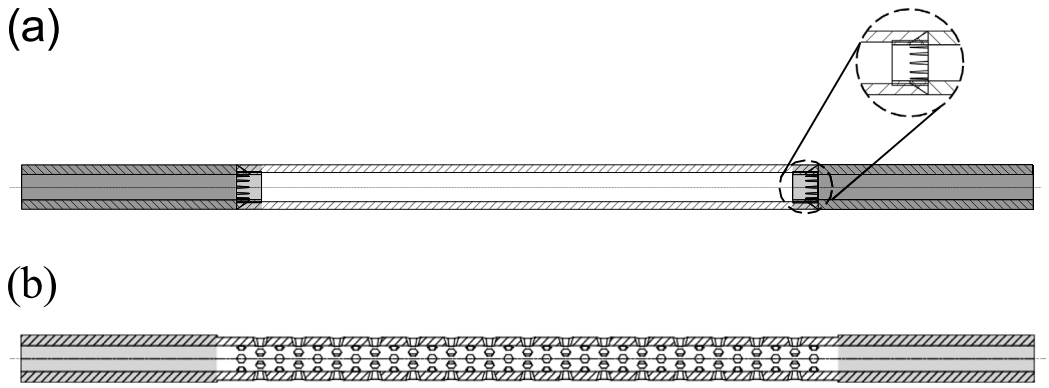

Fig. 1. Electrode design of (a) cathodes and (b) anodes and their gray-scaled functional domains. Solid ends (dark-gray) with a smooth finish provide proper sealing against O-rings. The center (white) is a porous gas diffusion section for the cathodes, whereas the anode is characterized by an open porous honeycomb grid. In case of the cathode, a sawtooth pattern (light gray), see detail view, ensures the gradual transition between the solid and the porous domains.

concepts are equally important for numbering-up tubular GDEs to assess the potential for large-scale application.

In this work, we present a scalable reactor for CO_2 electroreduction. 3D printed tubular copper GDEs are employed on the cathode side. Tubular membrane electrode assemblies (MEAs) made from stainless steel electrodes serve as anodes. Given the high adjustability of SLM, we design and manufacture electrodes with various domains fulfilling distinct functions. We further introduce a hybrid porosity GDE to improve CO_2 mass transfer to the catalyst surface. To assess catalytic performance under varying flow regimes, CO_2 electroreduction is conducted in both flow-through and flow-by mode. Eventually, the reactor is tested at high current densities of up to 500 mA cm^{-2}.

2. Material and methods

2.1. Electrode production

For electrode production, a laser powder bed fusion machine (MySint100 PM, Sisma S.p.A.) with a 200 W fiber laser was used. Print jobs were prepared in Magics 25.0.2.435 (Materialise NV) and processed with a SISMA build processor version 6.1.00001.0 (Materialise NV). Cathodes were printed from copper powder (Infinite powder Cu 01, Infinite Flex GmbH) having a medium particle diameter of 30 µm. A chessboard pattern was used, where laser power, hatching distance and scan speed were varied and the applied energy density was calculated accordingly. Details are available from our previous publication [28]. Anodes were printed from stainless steel powder (Laserform 316L (A), 3D Systems GmbH). Prior to every print job, the metal powders were sieved to a particle size below 60 µm. Fig. 1 shows the design of cathodes and anodes. Cathodes were printed with the dimensions 80.0 × 3.5 × 2.0 mm (length × outer diameter × inner diameter) and different functional domains, as pictured in Fig. 1(a). The center was realized as a porous GDE, whereas the ends were manufactured in a solid manner for O-ring sealing in the tubular reactor. Preliminary tests showed imperfections in the transition zone between porous and solid domains, which resulted in oversized pores affecting CO_2 gas flow and bubble formation on the electrode surface. For this reason, a sawtooth pattern was designed to provide a gradual transition in between the two domains, as highlighted in the detail view of Fig. 1(a). After printing, cathodes were cleaned for 10 min in an ultrasonic bath in isopropanol. Subsequently, the solid ends were treated with sandpaper to provide a smooth finish for sealing.

Anodes were printed with the dimensions 80.0 × 2.0 mm (length × inner diameter) and the outer diameter was varied for the center and the ends. As shown in Fig. 1(b), the center was designed with an open porous honeycomb grid, thereby realizing a surface porosity of about 31%. This allows anolyte on the lumen side to be in contact with Nafion™ tubing serving as cation exchange membrane, which was applied on the shell side of every anode. After printing, anodes were subjected to the same cleaning procedure as cathodes. The solid ends were processed on a lathe until reaching the outer diameter of the anode's center.

2.2. Preparation of membrane electrode assemblies

Tubular MEAs were prepared from the aforementioned stainless steel anodes and Nafion™ tubing (TT-110, Perma Pure) with about 2.18 mm inner diameter and a wall thickness of approximately 300 µm. A piece of Nafion™ tubing was stored in aqueous ethanol solution (80 Vol%) until swollen and gently put over a stainless steel anode. The tubing was centered on the anode to prevent a displacement during the shrinking process at ambient air. For solvent replacement, the readily prepared MEAs were subjected to a solvent exchange in deionized (DI) water and subsequently stored in DI water until use.

2.3. Physical characterization

Physical characterization of the electrodes included an optical evaluation via scanning electron microscopy (SEM) and microcomputed tomography (µCT), porosity determination and pore size distribution. For SEM imaging, electrodes were broken in liquid nitrogen and examined with a tabletop microscope (TM3030plus, Hitachi). µCT imaging was carried out on a high-resolution X-ray microscope (SkyScan 1272, Bruker). Porosity was calculated as per

$$\epsilon = 1 - \frac{m}{\rho_{Cu} \cdot V}\ , \tag{1}$$

with the porosity ϵ, electrode weight m, density of copper ρ_{Cu} (8960 kg m^{-3}) and electrode volume V. Determination of the pore size distribution was conducted on a gas-liquid porometer (POROLUX 1000, Porometer NV) after immersing the electrodes in a wetting fluid (Porefil, Porometer NV).

2.4. Reactor assembly and CO_2 electroreduction

The tubular reactor was printed from VeroClear™ (Stratasys) in a PolyJet 3D printer (Objet Eden 260 V, Stratasys). A drawing of the reactor can be found in Fig. 2. A copper cathode is placed in the center and surrounded by two MEAs with the Nafion™ tubing rendered in blue. For easy assembly, the reactor consists of three individual parts, namely one center part and two covers. The covers are screwed onto each end of the center part and proper tightness is ensured by O-rings placed into the corresponding grooves. The center part provides tube connectors for the catholyte flow while the covers hold the copper

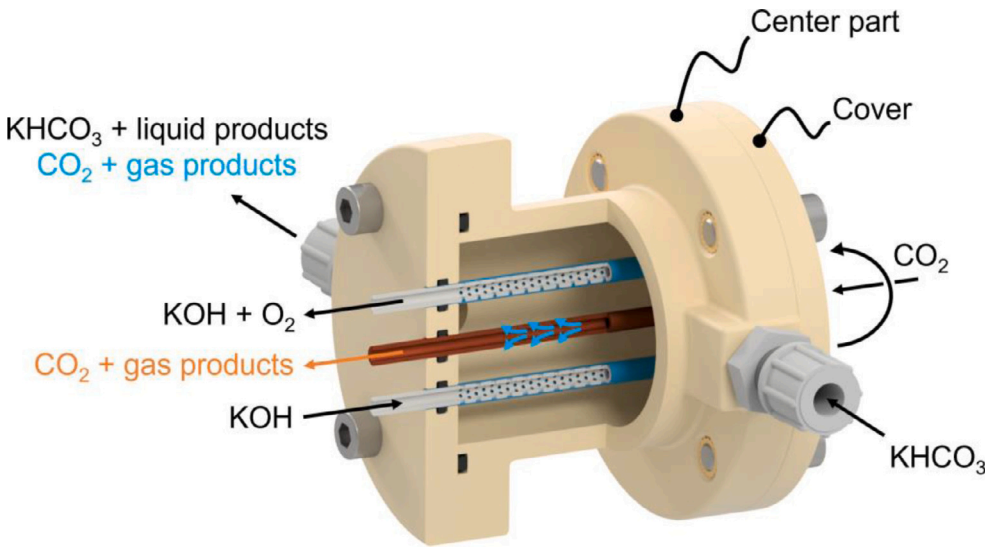

Fig. 2. CAD drawing of the reactor and involved material streams in both flow-through (blue) and flow-by (orange) mode. Material streams present in both modes are rendered in black. On the cathode side, $KHCO_3$ is cycled through the inner chamber of the reactor and CO_2 is fed into the lumen of the copper cathode. On the anode side, KOH is cycled through the lumen of the MEAs and O_2 from the OER is removed.

cathode and MEAs in place. O-rings inserted into the covers seal the catholyte compartment from the environment.

CO_2 electroreduction was performed under galvanostatic conditions using a potentiostat (SP-150, Biologic GmbH) coupled with a 20 A booster (Biologic GmbH). For electrical contact, crocodile clamps were attached on the accessible areas of the electrodes. The reactor was operated in both flow-through and flow-by mode, as pictured in Fig. 2. In flow-through mode, one end of the copper cathode was sealed. CO_2 humidified by a water column was forced from the lumen side through the porous electrode wall into the catholyte bulk. In flow-by mode, humidified CO_2 was channeled through the lumen side at a constant gas pressure of 100 mbar to prevent electrode flooding. Subsequently, the product gas was directed into the catholyte flask to collect catholyte that had potentially seeped through the electrode. For both operating modes, a CO_2 flow rate of 100 SmL min^{-1} was used. The reactor was operated in slightly tilted position, as pictured in Figure S1 (Supporting Information), to ensure best possible bubble removal.

An aqueous solution (0.5 mol L^{-1}) of potassium bicarbonate ($KHCO_3$, ≥ 99.7% purity, Carl Roth GmbH + Co. KG) served as catholyte. An aqueous solution (0.5 mol L^{-1}) of potassium hydroxide (KOH, Emplura®, Merck KGaA) was used as anolyte since stainless steel has been found to be a highly active OER material in alkaline media [39]. The catholyte was cycled through the catholyte chamber and, for equal starting conditions, saturated with CO_2 before every experiment. The anolyte was cycled through the lumen side of both MEAs connected in series. Oxygen (O_2) bubbles from the anodic oxygen evolution reaction (OER) were removed by the anolyte flow and phase-separated in the anolyte flask.

Product gas analysis was carried out with an online gas chromatograph (Agilent 8860, Agilent Technologies Inc.). A high performance liquid chromatograph (Agilent 1100 HPLC, Agilent Technologies Inc.) was used for analysis of the liquid products. Details regarding the calculation of the Faraday efficiencies can be found in Section S2 of the Supporting Information.

3. Results and discussion

3.1. Electrode production and physical characterization

Copper cathodes and MEAs were prepared as described in Sections 2.1 and 2.2. Fig. 3 shows photographs of the electrodes after each individual processing step. As can be seen in Fig. 3(a), the gas diffusion section in the center of the cathode is well discernible from the solid ends. Post-processing the ends with sandpaper renders a smooth surface for proper O-ring sealing, see Fig. 3(b). On the other hand, Fig. 3(c) presents a stainless steel anode with the open porous honeycomb grid. After machining the ends on a lathe, they have a smooth finish and the same diameter as the center section, see Fig. 3(d). The finish is necessary to provide good tightness between the anode shell surface and the Nafion™ tubing on top. A photograph of the readily prepared MEA is shown in Fig. 3(e). By combining additive manufacturing with traditional manufacturing methods, both cathodes and anodes were produced with high precision in a defined and reproducible manner.

For CO_2 electroreduction in the tubular reactor, three types of copper cathodes were manufactured with different laser hatching strategies, hereinafter designated as almost solid (AS), porous (P) and hybrid (H). Electrode H was designed as a hybrid of electrodes AS and P. An inner ring serving as gas distribution layer was printed with the laser hatching strategy of electrode AS. The gas distribution layer was supposed to evenly distribute CO_2 over the entire electrode. On top of the gas distribution layer, an outer ring functioning as high-surface layer was added with the laser hatching strategy of electrode P. The high-surface layer provides increased surface to maximize the amount of active sites for the CO_2RR. SEM images of the cross-sectional areas of electrodes AS, P and H are provided in Fig. 4. The two layers of electrode H can be well distinguished and are firmly bonded together. Fig. 5(a) shows the porosity of the three electrodes as a function of the energy density applied during the manufacturing process. Electrode AS was produced with an energy density of 1.25 J mm^{-2}, which leads to a comparably low porosity of about 12%. Electrode P is characterized by a higher porosity of approximately 24% as a result of the lower energy density (1.11 J mm^{-2}). With a porosity of about 22%, electrode H is close to electrode P, which can be explained by the proportions of the gas distribution layer (inner ring) and the high-surface layer (outer ring), see Fig. 4. The gas distribution layer makes up about 23% of the wall thickness with the remaining 77% available for the high-surface layer. Translated into the cross-sectional surface area, the high-surface layer, which corresponds to electrode P, takes about 82%. The remaining 18% are occupied by the gas distribution layer that matches electrode AS. As Fig. 5(b) implies, a similar behavior is also observed regarding the pore size distribution of the electrodes. With a main pore diameter of 5 μm, electrode H lies in between electrode AS (1 μm) and electrode P (8 μm). The results meet our expectations for a hybrid GDE that combines two porous domains in one body.

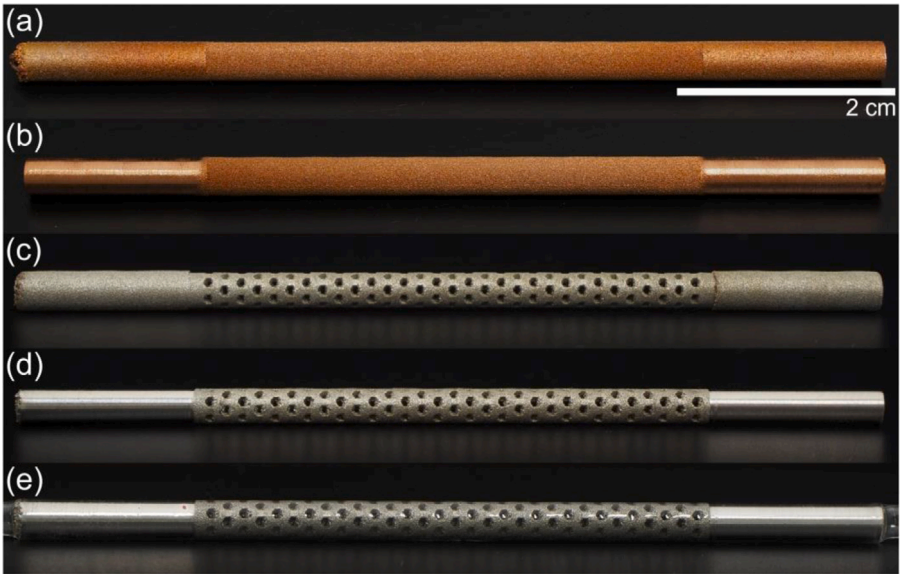

Fig. 3. Processing steps involved in cathode and anode production. (a) 3D printed cathode after removal of residual copper powder and (b) after polishing the solid ends to a smooth finish. (c) 3D printed anode after removal of residual stainless steel powder, (d) after turning the ends on a lathe and (e) after shrinking a commercial Nafion™ tubing, thereby creating a MEA.

For a three-dimensional insight into our electrodes, a hybrid electrode was examined using μCT imaging. Since electrode H was too dense for X-rays to penetrate the electrode wall, an additional electrode H2 was manufactured. The laser hatching strategy of electrode H2 was kept the same, but the high-surface layer was printed with a wider hatching distance (150 instead of 60 μm), which reduced X-ray shielding. Fig. 6 shows a μCT scan of electrode H2, more specifically, the transition zone between the porous center of the electrode and a solid end. As can be seen, gas distribution layer, high-surface layer and solid end are well discernible from each other. An additional cross-sectional view is provided in Figure S2 of the Supporting Information for a better resolution of the individual layers. Moreover, the sawtooth pattern applied for a gradual transition from solid end to porous center is visible in the cross-sectional view. Our findings demonstrate the successful production of hybrid porosity GDEs. Additive manufacturing is a promising approach for the realization of various domains, which fulfill distinct functions, in close proximity to each other.

3.2. CO_2 electroreduction

CO_2 electroreduction was performed in the tubular reactor according to the procedure introduced in Section 2.4. One copper cathode and two MEAs were plugged into the covers, as pictured in Fig. 7.

However, the reactor is not limited to three electrodes, but allows for scale-up by numbering-up the amount of cathodes and MEAs, or by increasing the reactor length. Moreover, electrodes can be arranged in different patterns to control flow conditions and formation of the electromagnetic field, which in turn affects ion migration and concentration of dissolved CO_2 [31]. The readily assembled reactor was operated with electrodes AS, P and H in both flow-through and flow-by mode. Fig. 8

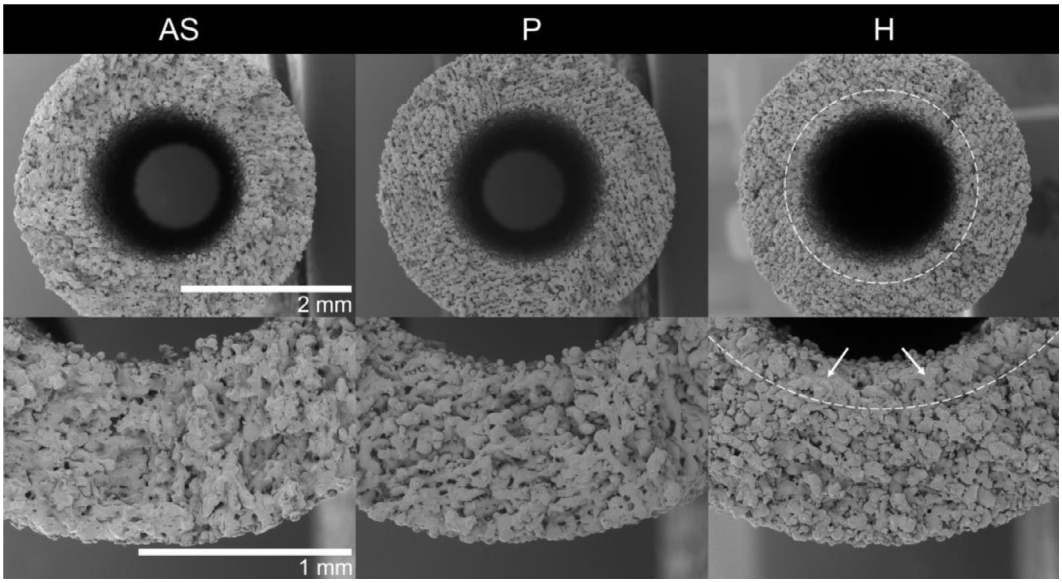

Fig. 4. Cross-sectional views of electrodes AS, P and H. Electrode H is a hybrid, where an inner and outer ring were manufactured with the laser hatching strategies of electrodes AS and P, respectively. White dashed lines represent the interface between inner and outer ring. White arrows in the close-up view of electrode H highlight the increased melting of copper particles due to a larger energy input in the inner ring.

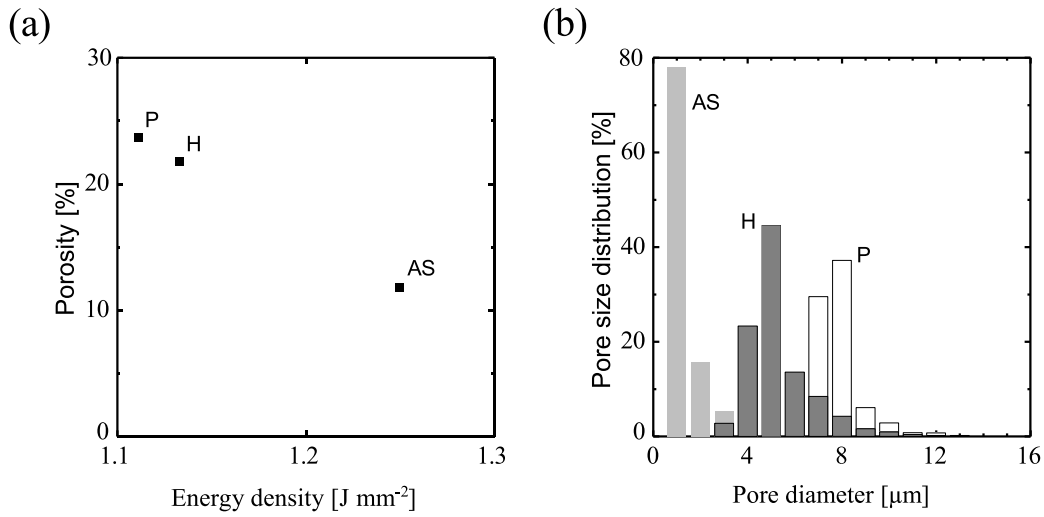

Fig. 5. (a) Porosity of electrodes AS, P and H over energy density applied during the manufacturing process. (b) Pore size distribution of the same electrodes as a function of the pore diameter measured via porometry.

shows the Faraday efficiencies reached for gaseous and liquid products in the two operating modes at 100 mA cm^{-2} current density.

In flow-through mode, see Fig. 8(a), the HER is predominant, but there is a striking difference in the catalytic behavior of the electrodes. CO, CH_4, ethylene (C_2H_4) and formic acid (HCOOH) are synthesized with all electrodes, but in different quantities. Electrode AS yields the least amount of products from the CO_2RR and the HER is most pronounced. However, with electrode P, the CO_2RR is amplified while the HER is mitigated, which is in accordance with the findings of our previous work [28]. By providing a larger ECSA on electrode P, more reaction sites are available for the CO_2RR. Going from electrode P to electrode H, however, the CO_2RR is boosted although electrode H is characterized by a smaller ECSA than electrode P, see Figure S3 (Supporting Information). The double layer capacitance of electrode H is in between the values of electrodes P and AS, which matches the results from porosity determination and pore size distribution. In spite of linking the better performance of electrode H only to the available ECSA, we suggest the hybrid structure to have a beneficial effect on CO_2 supply. By integration of the gas distribution layer (inner ring), CO_2 is distributed more evenly, which leads to a higher amount of dissolved CO_2 in the catalyst vicinity. A difference in wetting behavior can be excluded as possible explanation for the presented results. Electrodes P and H show similar wetting behavior, see Figure S4 (Supporting Information). This observation is in line with our expectations since the high-surface layer (outer ring) of electrode H matches electrode P, which is in contact with the catholyte.

In contrast to flow-through mode, all electrodes performed significantly worse in flow-by mode. As can be concluded from Fig. 8(b), the HER is by far the most pronounced reaction with more than 90% Faraday efficiency in all cases. This is likely to be caused by the large wall thickness, which amounts to 750 µm for every electrode and exceeds common values reported for gas diffusion layers of planar GDEs [40,41]. Long diffusion pathways from the lumen side into the pore network result in CO_2 mass transfer limitations, which provoke an increase of the HER. In addition, a change in product distribution is observed in flow-by mode, where almost exclusively CH_4 is formed. This might be due to a higher surface coverage of reaction intermediates on the catalyst surface. In contrast to CO and HCOOH formation (two-electron transfer), CH_4 formation involves eight electrons and more reaction intermediates [42]. The flow-by mode is governed by diffusive mass transfer from the lumen side into the pore network, whereas in flow-through mode convection is the governing transport mechanism. For this reason, the adsorption of reaction intermediates is more pronounced in flow-by mode, which predominantly yields CH_4 in the product gas.

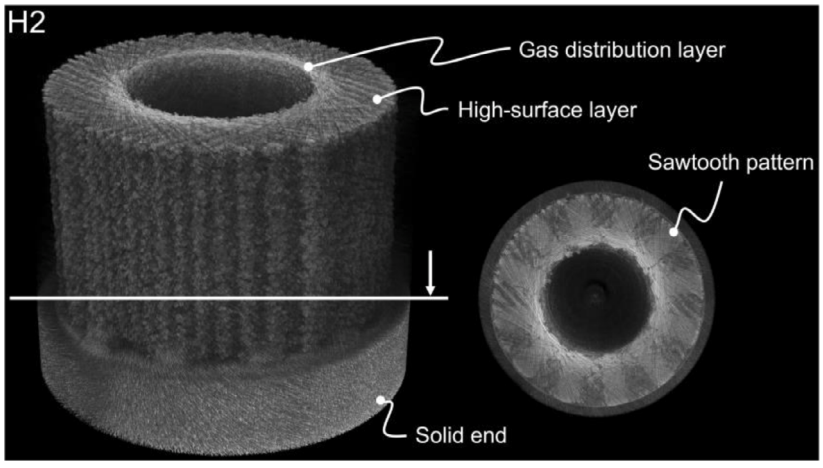

Fig. 6. µCT scan of electrode H2 with a cross-sectional view of the transition zone, which allows a deeper insight into the electrode. Gas distribution layer, high-surface layer, solid end and sawtooth pattern can be clearly distinguished from each other.

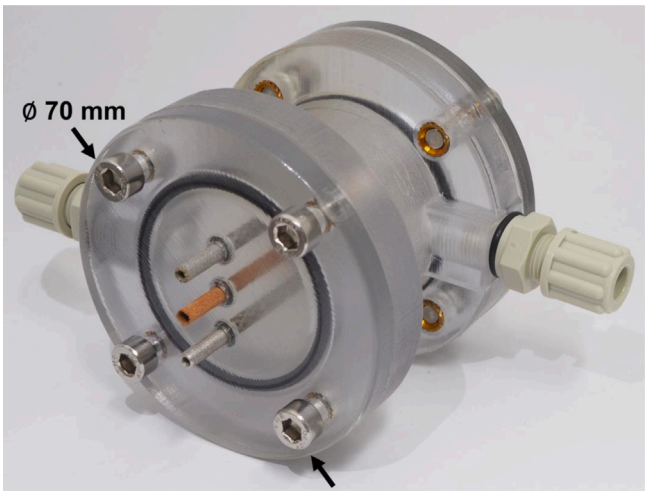

Fig. 7. Photograph of the readily assembled reactor.

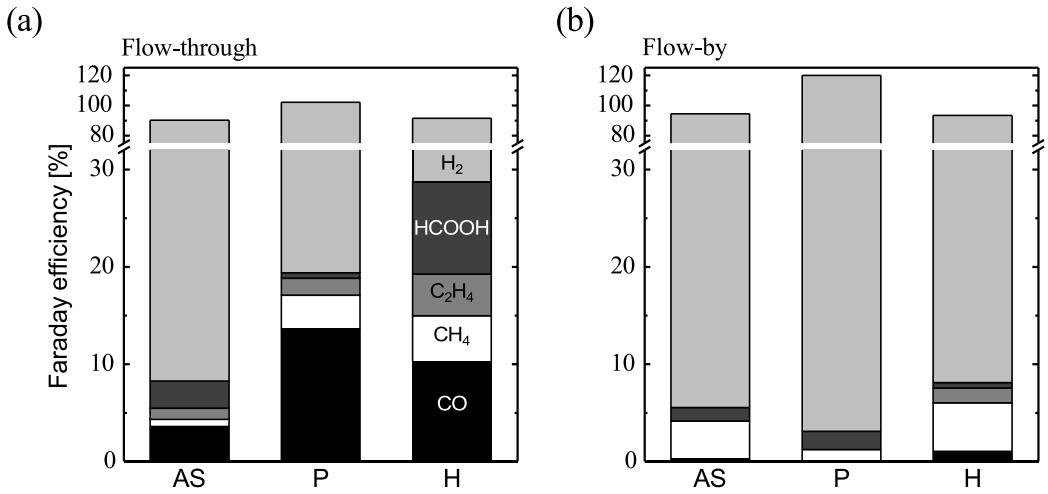

Fig. 8. Faraday efficiencies reached for (a) flow-through and (b) flow-by mode using electrodes AS, P and H at 100 mA cm^{-2} current density. In both modes, the CO_2RR is most pronounced with electrode H. However, for all electrodes the CO_2RR is diminished in flow-by mode and a change in product distribution can be observed. Operating the electrodes in flow-by mode favors CH_4 formation, which might stem from a higher surface coverage of reaction intermediates on the catalyst surface.

To assess the tubular reactor at industrially relevant current densities, further experiments were carried out with electrode H in flow-through mode. Aside from the already discussed data at 100 mA cm^{-2}, Fig. 9 shows the Faraday efficiencies for 200 and 500 mA cm^{-2}. Increasing the current density to 200 mA cm^{-2} results in a rising HER and decreasing CO_2RR. The formation of CH_4 and C_2H_4 is affected most, whereas CO and HCOOH are still synthesized. The effect is even more pronounced at 500 mA cm^{-2}, where hydrogen is formed almost exclusively. At 500 mA cm^{-2}, a CO_2 excess of 5.7 was applied based on a two-electron transfer reaction. Nevertheless, the high amount of supplied CO_2 does not seem to be enough for conversion of CO_2 to value-added products. Further optimization of the pore network is necessary to tackle CO_2 mass transfer limitation and diminish the HER at such high current densities.

4. Conclusions

The characterization of tubular GDEs under changing conditions and different flow regimes requires new concepts. Only by incorporating tubular GDEs in suitable reactors, the scale-up of tubular systems can be realized in the future. In this work, we presented a continuous flow reactor with copper GDEs and MEAs made from stainless steel anodes surrounded by commercially available Nafion™ tubing.

Additive manufacturing coupled with traditional manufacturing methods proved to be a good approach to produce electrodes with high precision and in a reproducible manner. Moreover, a hybrid porosity electrode was realized, which combines different domains in close proximity to each other. Through μCT imaging, the successful production of these domains could be confirmed and visualized.

In flow-through mode, the hybrid electrode outperformed other electrodes, which we explain with an enhanced CO_2 mass transfer to the catalyst surface. In flow-by mode, all electrodes performed worse and the HER dominated, most probably due to the large electrode wall thickness and long diffusion pathways. However, a shift to CH_4 formation could be observed, which was associated to higher surface coverage of reaction intermediates on the catalyst surface. While in flow-through mode CO_2 is actively forced through the porous electrodes walls, flow-by mode is characterized by diffusion as the governing transport mechanism. The reactor was successfully operated at high current densities up to 500 mA cm^{-2} and allows for assessment of further operating points in the future.

Nonetheless, electrodes and reactors must be optimized for highly efficient synthesis of value-added compounds. On the one hand, the development of copper GDEs with a thinner wall thickness should be focused. In this way, diffusion pathways could be shortened, thereby preventing CO_2 mass transfer limitations, especially in flow-by mode.

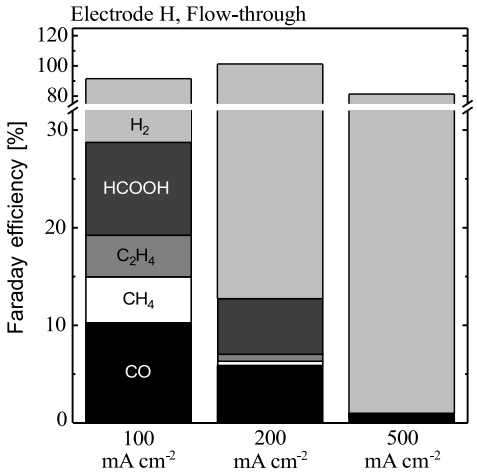

Fig. 9. Faraday efficiencies for electrode H in flow-through mode at 100 SmL min^{-1} CO_2 flow rate and different current densities. With increasing current density, the CO_2RR is supressed, which is caused by CO_2 mass transfer limitation to the catalyst surface.

On the other hand, different electrode arrays should be evaluated to identify favorable layouts.

CRediT authorship contribution statement

Nils Weber: Conceptualization, Data curation, Formal analysis, Investigation, Methodology, Project administration, Software, Supervision, Validation, Visualization, Writing – original draft, Writing – review & editing, Funding acquisition. **Max Möntmann:** Data curation, Formal analysis, Investigation, Software, Visualization. **Matthias Wessling:** Conceptualization, Funding acquisition, Methodology, Project administration, Resources, Supervision, Visualization, Writing – original draft, Writing – review & editing. **Robert Keller:** Conceptualization, Data curation, Formal analysis, Funding acquisition, Methodology, Project administration, Supervision, Validation, Visualization, Writing – original draft, Writing – review & editing.

Declaration of competing interest

The authors declare that they have no known competing financial interests or personal relationships that could have appeared to influence the work reported in this paper.

Data availability

Data will be made available on request.

Acknowledgments

The authors wish to thank Alexander Limper, Tobias Harhues, Caroline Schmitz, Timo Linzenmeier, Justin Gottfried, Karin Faensen and Anselm Brodersen for their kind support.

M.W. acknowledges DFG, Germany funding through the Gottfried Wilhelm Leibniz Award 2019 (WE 4678/12-1). N.W. acknowledges funding by the Deutsche Forschungsgemeinschaft, Germany (DFG, German Research Foundation) under Germany's Excellence Strategy – Cluster of Excellence 2186 "The Fuel Science Center" – ID: 390919832. The SLM printer was funded under the same grant through the Junior Research Group CA2-JRG, Germany.

This work was conducted in part at the Competence Center for Industrial Electrochemistry ELECTRA, which is supported by the "European Regional Development Fund (ERDF)" and the Federal State of North Rhine-Westphalia, Germany (grant no. ERDF 05 00 07 7).

Appendix A. Supplementary data

Supplementary material related to this article can be found online at https://doi.org/10.1016/j.cej.2024.150031.

References

[1] A. Kumar, L.M. Aeshala, T. Palai, Electrochemical reduction of CO_2 to useful fuel: recent advances and prospects, J. Appl. Electrochem. 53 (7) (2023) 1295–1319, http://dx.doi.org/10.1007/s10800-023-01850-x.

[2] S.C. Peter, Reduction of CO_2 to Chemicals and Fuels: A Solution to Global Warming and Energy Crisis, ACS Energy Lett. 3 (7) (2018) 1557–1561, http://dx.doi.org/10.1021/acsenergylett.8b00878.

[3] R. Kas, K.K. Hummadi, R. Kortlever, P. De Wit, A. Milbrat, M.W. Luiten-Olieman, N.E. Benes, M.T. Koper, G. Mul, Three-dimensional porous hollow fibre copper electrodes for efficient and high-rate electrochemical carbon dioxide reduction, Nature Commun. 7 (2016) 1–7, http://dx.doi.org/10.1038/ncomms10748.

[4] D. Bell, D. Rall, M. Großeheide, L. Marx, L. Hülsdünker, M. Wessling, Tubular hollow fibre electrodes for CO_2 reduction made from copper aluminum alloy with drastically increased intrinsic porosity, Electrochem. Commun. 111 (2020) http://dx.doi.org/10.1016/j.elecom.2019.106645.

[5] K.K. Hummadi, A. Sustronk, R. Kas, N. Benes, G. Mul, Optimizing temperature treatment of copper hollow fibers for the electrochemical reduction of CO_2 to CO, Catalysts 11 (5) (2021) http://dx.doi.org/10.3390/catal11050571.

[6] A.C. Sustronk, N.E. Benes, G. Mul, Conversion of a CO–CO_2 co-feed with a porous tubular copper catalyst at low potential, Electrochem. Sci. Adv. 3 (2) (2023) 1–6, http://dx.doi.org/10.1002/elsa.202100198.

[7] C. Zhu, G. Shen, W. Chen, X. Dong, G. Li, Y. Song, W. Wei, Y. Sun, Copper hollow fiber electrode for efficient CO_2 electroreduction, J. Power Sources 495 (January) (2021) 229814, http://dx.doi.org/10.1016/j.jpowsour.2021.229814.

[8] D. Liu, Y. Hu, E. Shoko, H. Yu, T.T. Isimjan, X. Yang, High selectivity of CO_2 conversion to formate by porous copper hollow fiber: Microstructure and pressure effects, Electrochim. Acta 365 (2021) 137343, http://dx.doi.org/10.1016/j.electacta.2020.137343.

[9] C. Zhu, Y. Song, X. Dong, G. Li, A. Chen, W. Chen, G. Wu, S. Li, W. Wei, Y. Sun, Ampere-level CO_2 reduction to multicarbon products over a copper gas penetration electrode, Energy Environ. Sci. 15 (12) (2022) 5391–5404, http://dx.doi.org/10.1039/d2ee02121h.

[10] G. Li, Y. Song, C. Zhu, X. Dong, W. Chen, G. Wu, G. Feng, S. Li, W. Wei, Facet-oriented Cu_2 O and oxygen vacancies synergistically promoting CO_2 electroreduction to formate on Cu-based hollow fiber, J. CO_2 Util. 70 (February) (2023) 102446, http://dx.doi.org/10.1016/j.jcou.2023.102446.

[11] B. Chen, J. Xu, J. Zou, D. Liu, Y. Situ, H. Huang, Formate-Selective CO_2 Electrochemical Reduction with a Hydrogen-Reduction-Suppressing Bronze Alloy Hollow-Fiber Electrode, ChemSusChem 13 (24) (2020) 6594–6601, http://dx.doi.org/10.1002/cssc.202002314.

[12] X. Dong, G. Li, W. Chen, C. Zhu, T. Li, Y. Song, N. Sun, W. Wei, Gas-phase CO_2 electroreduction over Sn-Cu hollow fibers, Mater. Adv. 2 (1) (2021) 241–247, http://dx.doi.org/10.1039/d0ma00851f.

[13] H. Rabiee, X. Zhang, L. Ge, S. Hu, M. Li, S. Smart, Z. Zhu, Z. Yuan, Tuning the Product Selectivity of the Cu Hollow Fiber Gas Diffusion Electrode for Efficient CO_2 Reduction to Formate by Controlled Surface Sn Electrodeposition, ACS Appl. Mater. Interfaces 12 (19) (2020) 21670–21681, http://dx.doi.org/10.1021/acsami.0c03681.

[14] I. Merino-Garcia, J. Albo, P. Krzywda, G. Mul, A. Irabien, Bimetallic Cu-based hollow fibre electrodes for CO_2 electroreduction, Catalysis Today 346 (February) (2020) 34–39, http://dx.doi.org/10.1016/j.cattod.2019.03.025.

[15] H. Rabiee, L. Ge, X. Zhang, S. Hu, M. Li, S. Smart, Z. Zhu, Z. Yuan, Shape-tuned electrodeposition of bismuth-based nanosheets on flow-through hollow fiber gas diffusion electrode for high-efficiency CO_2 reduction to formate, Appl. Catal. B 286 (November 2020) (2021) 119945, http://dx.doi.org/10.1016/j.apcatb.2021.119945.

[16] H. Rabiee, L. Ge, X. Zhang, S. Hu, M. Li, S. Smart, Z. Zhu, H. Wang, Z. Yuan, Stand-alone asymmetric hollow fiber gas-diffusion electrodes with distinguished bronze phases for high-efficiency CO_2 electrochemical reduction, Appl. Catal. B 298 (May) (2021) 120538, http://dx.doi.org/10.1016/j.apcatb.2021.120538.

[17] H. Rabiee, J.K. Heffernan, L. Ge, X. Zhang, P. Yan, E. Marcellin, S. Hu, Z. Zhu, H. Wang, Z. Yuan, Tuning flow-through Cu-based hollow fiber gas-diffusion electrode for high-efficiency carbon monoxide (CO) electroreduction to C2+products, Appl. Catal. B 330 (February) (2023) 122589, http://dx.doi.org/10.1016/j.apcatb.2023.122589.

[18] X. Zhao, Y. Song, S. Yang, W. Chen, T. Li, G. Wu, S. Li, G. Li, X. Dong, Z. Jiang, W. Wei, Y. Sun, Ni Hollow Fiber Encapsulated Bi@Zeolite for Efficient CO_2 Electroreduction, ACS Applied Energy Materials (2021) http://dx.doi.org/10.1021/acsaem.1c01195.

[19] M.Y. Lee, S. Han, H. Lim, Y. Kwon, S. Kang, Electrocatalytic CO_2 Reduction via a Permeable CNT Hollow-Fiber Electrode Incorporated with SnO_2 Nanoparticles, ACS Sustain. Chem. Eng. 8 (5) (2020) 2117–2121, http://dx.doi.org/10.1021/acssuschemeng.9b05701.

[20] M.Y. Lee, S. Ringe, H. Kim, S. Kang, Y. Kwon, Electric field mediated selectivity switching of electrochemical CO_2 reduction from formate to CO on carbon supported Sn, ACS Energy Lett. 5 (9) (2020) 2987–2994, http://dx.doi.org/10.1021/acsenergylett.0c01387.

[21] B. Bian, M.F. Alqahtani, K.P. Katuri, D. Liu, S. Bajracharya, Z. Lai, K. Rabaey, P.E. Saikaly, Porous nickel hollow fiber cathodes coated with CNTs for efficient microbial electrosynthesis of acetate from CO_2 using: Sporomusa ovata, J. Mater. Chem. A 6 (35) (2018) 17201–17211, http://dx.doi.org/10.1039/c8ta05322g.

[22] M.F. Alqahtani, K.P. Katuri, S. Bajracharya, Y. Yu, Z. Lai, P.E. Saikaly, Porous Hollow Fiber Nickel Electrodes for Effective Supply and Reduction of Carbon Dioxide to Methane through Microbial Electrosynthesis, Adv. Funct. Mater. 28 (43) (2018) 1–8, http://dx.doi.org/10.1002/adfm.201804860.

[23] B. Bian, Y. Singh, K. Rabaey, P.E. Saikaly, Nickel-Coated ceramic hollow fiber cathode for fast enrichment of chemolithoautotrophs and efficient reduction of CO_2 in microbial electrosynthesis, Chem. Eng. J. 450 (P3) (2022) 138230, http://dx.doi.org/10.1016/j.cej.2022.138230.

[24] S. Li, X. Dong, W. Chen, Y. Song, G. Li, W. Wei, Y. Sun, Efficient CO_2 Electroreduction over Silver Hollow Fiber Electrode, Catalysts 12 (5) (2022) 1–11, http://dx.doi.org/10.3390/catal12050453.

[25] S. Li, X. Dong, Y. Zhao, J. Mao, W. Chen, A. Chen, Y. Song, G. Li, Z. Jiang, W. Wei, Y. Sun, Chloride Ion Adsorption Enables Ampere-Level CO_2 Electroreduction over Silver Hollow Fiber, Angew. Chem. Int. Edn 61 (42) (2022) 1–5, http://dx.doi.org/10.1002/anie.202210432.

[26] S. Li, W. Chen, X. Dong, C. Zhu, A. Chen, Y. Song, G. Li, W. Wei, Y. Sun, Hierarchical micro/nanostructured silver hollow fiber boosts electroreduction of carbon dioxide, Nature Commun. 13 (1) (2022) http://dx.doi.org/10.1038/s41467-022-30733-6.

[27] X. Dong, S. Li, C. Zhu, J. Mao, G. Wu, G. Li, G. Feng, A. Chen, Y. Wei, X. Liu, J. Wang, Y. Song, W. Chen, W. Wei, Highly efficient ampere-level CO_2 reduction to multicarbon products via stepwise hollow-fiber penetration electrodes, Appl. Catal. B 336 (March) (2023) 122929, http://dx.doi.org/10.1016/j.apcatb.2023.122929.

[28] N. Weber, J. Linkhorst, R. Keller, M. Wessling, Tailoring Pore Networks – Gas Diffusion Electrodes via Additive Manufacturing, Adv. Mater. Technol. 2300720 (2023) 1–8, http://dx.doi.org/10.1002/admt.202300720.

[29] A. Limper, N. Weber, A. Brodersen, R. Keller, M. Wessling, J. Linkhorst, Additive manufacturing of composite porosity mixer electrodes, Electrochem. Commun. 134 (December 2021) (2022) 107176, http://dx.doi.org/10.1016/j.elecom.2021.107176.

[30] I. Bagemihl, C. Bhatraju, J.R. Van Ommen, V. Van Steijn, Electrochemical Reduction of CO_2 in Tubular Flow Cells under Gas-Liquid Taylor Flow, ACS Sustain. Chem. Eng. 10 (38) (2022) 12580–12587, http://dx.doi.org/10.1021/acssuschemeng.2c03038.

[31] K.M. Diederichsen, S.J. DeWitt, T.A. Hatton, Electrochemically Facilitated Transport of CO_2 between Gas Diffusion Electrodes in Flat and Hollow Fiber Geometries, ACS ES T Eng. (2023) http://dx.doi.org/10.1021/acsestengg.3c00030.

[32] J.B. Vennekoetter, R. Sengpiel, M. Wessling, Beyond the catalyst: How electrode and reactor design determine the product spectrum during electrochemical CO_2 reduction, Chem. Eng. J. 364 (January) (2019) 89–101, http://dx.doi.org/10.1016/j.cej.2019.01.045.

[33] S.C. Perry, C. Ponce de León, F.C. Walsh, Review—The Design, Performance and Continuing Development of Electrochemical Reactors for Clean Electrosynthesis, J. Electrochem. Soc. 167 (15) (2020) 155525, http://dx.doi.org/10.1149/1945-7111/abc58e.

[34] D. Ma, T. Jin, K. Xie, H. Huang, An overview of flow cell architecture design and optimization for electrochemical CO_2 reduction, J. Mater. Chem. A 9 (37) (2021) 20897–20918, http://dx.doi.org/10.1039/d1ta06101a.

[35] M. Duarte, B. De Mot, J. Hereijgers, T. Breugelmans, Electrochemical Reduction of CO_2 : Effect of Convective CO_2 Supply in Gas Diffusion Electrodes, ChemElectroChem 6 (22) (2019) 5596–5602, http://dx.doi.org/10.1002/celc.201901454.

[36] M. Heßelmann, B.C. Bräsel, R.G. Keller, M. Wessling, Simulation-based guidance for improving CO_2 reduction on silver gas diffusion electrodes, Electrochem. Sci. Adv. 3 (1) (2023) 2100160, http://dx.doi.org/10.1002/elsa.202100160.

[37] M. Großeheide, D. Schaffeld, R. Keller, M. Wessling, A falling film design for electrochemical CO_2 reduction, Electrochem. Commun. 150 (April) (2023) 0–4, http://dx.doi.org/10.1016/j.elecom.2023.107487.

[38] M. Filippi, T. Möller, L. Liang, P. Strasser, Understanding the Impact of Catholyte Flow Compartment Design on the Efficiency of CO_2 Electrolyzers, Energy Environ. Sci. (2023) http://dx.doi.org/10.1039/d3ee02243a.

[39] F. Moureaux, P. Stevens, G. Toussaint, M. Chatenet, Timely-activated 316L stainless steel: A low cost, durable and active electrode for oxygen evolution reaction in concentrated alkaline environments, Applied Catalysis B: Environmental, vol. 258, 2019, pp. 1–35, http://dx.doi.org/10.1016/j.apcatb.2019.117963.

[40] Y. Wu, S. Garg, M. Li, M.N. Idros, Z. Li, R. Lin, J. Chen, G. Wang, T.E. Rufford, Effects of microporous layer on electrolyte flooding in gas diffusion electrodes and selectivity of CO_2 electrolysis to CO, J. Power Sources 522 (January) (2022) 230998, http://dx.doi.org/10.1016/j.jpowsour.2022.230998.

[41] A.A. Samu, I. Szenti, Á. Kukovecz, B. Endrődi, C. Janáky, Systematic screening of gas diffusion layers for high performance CO_2 electrolysis, Commun. Chem. 6 (1) (2023) 1–9, http://dx.doi.org/10.1038/s42004-023-00836-2.

[42] Y.Y. Birdja, E. Pérez-Gallent, M.C. Figueiredo, A.J. Göttle, F. Calle-Vallejo, M.T. Koper, Advances and challenges in understanding the electrocatalytic conversion of carbon dioxide to fuels, Nature Energy 4 (9) (2019) 732–745, http://dx.doi.org/10.1038/s41560-019-0450-y.